AMERICAN SOCIETY FOR MICROBIOLOGY | Microbiology Spectrum

RESEARCH ARTICLE

Nitrite Promotes ROS Production to Potentiate Cefoperazone-Sulbactam-Mediated Elimination to Lab-Evolved and Clinical-Evolved *Pseudomonas aeruginosa*

Su-fang Kuang,[a] Xia Li,[a] Ding-Yun Feng,[a] Wen-Bin Wu,[a] Hui Li,[a,b] Bo Peng,[a,b] Xuan-xian Peng,[a,b] Zhuang-gui Chen,[a] Tian-tuo Zhang[a]

[a]The Third Affiliated Hospital and State Key Laboratory of Bio-Control, School of Life Sciences, Southern Marine Science and Engineering Guangdong Laboratory (Zhuhai), Sun Yat-sen University, University City, Guangzhou, People's Republic of China

[b]Laboratory for Marine Fisheries Science and Food Production Processes, Qingdao National Laboratory for Marine Science and Technology, Qingdao, China

ABSTRACT Cefoperazone-sulbactam (SCF)-resistant *Pseudomonas aeruginosa* poses a big challenge in the use of SCF to treat infection caused by the pathogen. We have recently shown exogenous nitrite-enabled killing of naturally and artificially evolved *Pseudomonas aeruginosa* strains (AP-$R_{CLIN\text{-}EVO}$ and AP-$R_{LAB\text{-}EVO}$, respectively) by SCF. However, the underlying mechanism is unknown. Here, reprogramming metabolomics was adopted to investigate how nitrite enhanced the SCF-mediated killing efficacy. Nitrite-reprogrammed metabolome displayed an activated pyruvate cycle (P cycle), which was confirmed by elevated activity of pyruvate dehydrogenase (PDH), α-ketoglutarate dehydrogenase, succinate dehydrogenase, and malate dehydrogenase. The activated P cycle provided NADH for the electron transport chain and thereby increased reactive oxygen species (ROS), which potentiated SCF to kill AP-$R_{CLIN\text{-}EVO}$ and AP-$R_{LAB\text{-}EVO}$. The nitrite-enabled killing of AP-$R_{CLIN\text{-}EVO}$ and AP-$R_{LAB\text{-}EVO}$ by SCF was inhibited by PDH inhibitor furfural and ROS scavenger N-Acetyl-L-cysteine but promoted by ROS promoter Fe^{3+}. SCF alone could not induce ROS, but SCF-mediated killing efficacy was enhanced by ROS. In addition, the present study demonstrated that nitrite repressed antioxidants, which were partly responsible for the elevated ROS. These results reveal a nitrite-reprogrammed metabolome mechanism by which AP-$R_{CLIN\text{-}EVO}$ and AP-$R_{LAB\text{-}EVO}$ sensitivity to SCF is elevated.

IMPORTANCE Antibiotic-resistant *Pseudomonas aeruginosa* has become a real concern in hospital-acquired infections, especially in critically ill and immunocompromised patients. Understanding antibiotic resistance mechanisms and developing novel control measures are highly appreciated. We have recently shown that a reduced nitrite-dependent NO biosynthesis contributes to cefoperazone-sulbactam (SCF) resistance, which is reverted by exogenous nitrite, in both naturally and artificially evolved *P. aeruginosa* strains (AP-$R_{CLIN\text{-}EVO}$ and AP-$R_{LAB\text{-}EVO}$, respectively). However, the mechanism is unknown. The present study reports that the nitrite-enabled killing of AP-$R_{CLIN\text{-}EVO}$ and AP-$R_{LAB\text{-}EVO}$ by SCF is attributed to the promoted production of reactive oxygen species (ROS). Nitrite activates the pyruvate cycle to generate NADH for the electron transport chain, which in turn promotes ROS generation. Nitrite-potentiated SCF-mediated killing is decreased by pyruvate dehydrogenase inhibitor furfural and ROS scavenger N-Acetyl-L-cysteine but increased by ROS promoter Fe^{3+}. Furthermore, SCF-mediated killing is promoted by H_2O_2 in a dose-dependent manner. In addition, the combination of nitrite and H_2O_2 greatly enhances SCF-mediated killing. These results not only disclose a nitrite-ROS-potentiated SCF-mediated killing, but also show SCF-mediated killing is dependent upon ROS.

KEYWORDS *Pseudomonas aeruginosa*, antibiotic resistance, cefoperazone-sulbactam, electron transport chain, nitrite, reprogramming metabolomics, the pyruvate cycle

Editor Adriana E. Rosato, Riverside University Health System, Medical Center – University of California

Address correspondence to Tian-tuo Zhang, zhtituli@163.com.

The authors declare no conflict of interest.

Received 26 November 2021
Accepted 15 June 2022
Published 5 July 2022

Pseudomonas aeruginosa is an opportunistic pathogen that causes severe infections in humans, especially in cystic fibrosis patients. Antibiotic-resistant *P. aeruginosa* isolates are frequently isolated in clinic and environments since it rapidly develops multidrug resistance under antibiotic selective pressure (1, 2). These resistant strains are insensitive to most classes of antibiotics. However, no new antibiotics are available to combat the growing threat of the antibiotic resistance. Therefore, combating these multidrug-resistant *P. aeruginosa* is an urgent issue in clinical practice.

P. aeruginosa has the ability to adapt to its environment through a versatile energy metabolism network (3), suggesting that this bacterium may manipulate metabolism to cope with antibiotic stress. Han et al. used a metabolomics approach in combination with lipidomics or transcriptomics to investigate polymyxin-resistant *P. aeruginosa*. They showed that polymyxin treatment causes significant perturbations in the biosynthesis of lipids, lipopolysaccharide and peptidoglycan, central carbon metabolism, and oxidative stress. They proposed decreased phospholipid level as a consequence of polymyxin resistance (4, 5). Hussein et al. utilized untargeted metabolomics to investigate the mechanism(s) of synergy between polymyxin B and tamoxifen or sertraline against polymyxin-resistant multidrug-resistant (MDR) cystic fibrosis (CF) *P. aeruginosa* isolates. The primary mechanisms with tamoxifen involve disruption of cell envelope biogenesis and inhibition of lipopolysaccharide (LPS) modifications. In combination with sertraline, polymyxin B impairs glycerophospholipids and fatty acids and the pantothenate and coenzyme A pathways (6, 7). These studies may provide valuable information about metabolic pathways leading to an understanding of the adaptations of bacterial strains to antibiotic stress.

Recently developed reprogramming metabolomics can identify crucial biomarkers to revert or restore metabolomes against stresses (8–12), including antibiotic-resistant metabolomes reprogrammed to antibiotic-sensitive metabolomes to potentiate antibiotic-mediated killing efficacy (13–18). In a recent study, we have adopted an approach to investigate metabolic profiles in naturally and artificially evolved strains carrying cefoperazone-sulbactam (SCF) resistance (AP-$R_{CLIN-EVO}$ and AP-$R_{LAB-EVO}$, respectively) from the same parental strain (AP-R_{CLIN}). AP-R_{CLIN} and AP-$R_{CLIN-EVO}$ are isolated from lower respiratory secretions of the patient by using a bronchofiberscope at 3-day intervals. AP-$R_{LAB-EVO}$ is obtained through sequential propagation of AP-R_{CLIN} in medium with SCF. Reduced NO is identified as an overlapped characteristic feature of the two evolved strains, which is attributed to nitrite-dependent NO biosynthesis instead of an arginine-dependent NO pathway. Exogenous nitrite promotes NO and thereby potentiates SCF-mediated killing (19). However, the mechanism underlying the nitrite-potentiated killing is unknown.

Here, gas chromatography-mass spectrometry (GC-MS) based metabolomics are used to compare metabolic profiles between nitrite-induced and control metabolomes to understand the metabolic differences. We demonstrate that nitrite-potentiated SCF-mediated killing is attributed to promotion of ROS and SCF is a ROS-dependent antibiotic.

RESULTS

Nitrite-induced metabolic profiles in AP-$R_{CLIN-EVO}$ and AP-$R_{LAB-EVO}$. AP-$R_{CLIN-EVO}$ and AP-$R_{LAB-EVO}$ were cultured in medium with and without nitrite and designed as N-AP-$R_{CLIN-EVO}$, N-AP-$R_{LAB-EVO}$ and AP-$R_{CLIN-EVO}$, AP-$R_{LAB-EVO,}$ respectively. Then, GC-MS-based metabolomics were adopted to characterize nitrite-induced metabolic profiles in N-AP-$R_{CLIN-EVO}$ and N-AP-$R_{LAB-EVO}$ compared to those of AP-$R_{CLIN-EVO}$ and AP-$R_{LAB-EVO}$, respectively. Four biological samples with two technical replicates were performed for each group, yielding a total of 32 data sets. A total of 230 aligned individual peaks were achieved (Fig. 1A). The correlation coefficients between technical duplication varied between 0.95 and 0.99, indicating the reproducibility of the data (Fig. 1B). After removing the internal standard ribitol and any known artificial peaks, 70 metabolites were identified at each sample. N-AP-$R_{CLIN-EVO}$ and N-AP-$R_{LAB-EVO}$ were first clustered together and then with AP-$R_{LAB-EVO}$ and last with AP-$R_{CLIN-EVO}$ (Fig. 1C). As shown in the metabolite classification chart, the proportions of carbohydrate, amino acid, lipid, nucleotide,

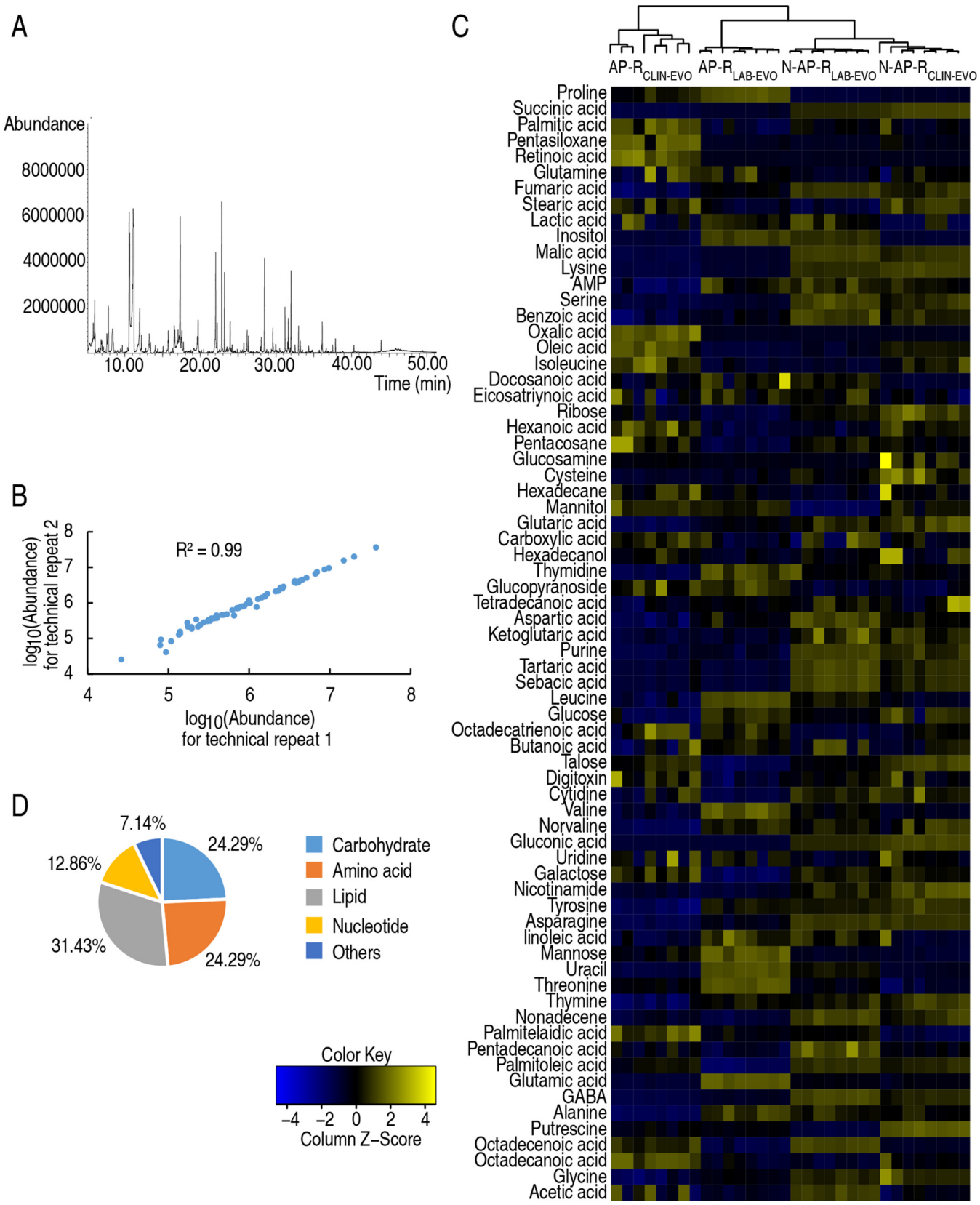

FIG 1 Metabolic profiles between nitrite-induced metabolomics in AP-$R_{CLIN-EVO}$ and AP-$R_{LAB-EVO}$. (A) Representative total ion current chromatogram. (B) Pearson correlation coefficient between technical replicates. (C) Heat map of unsupervised hierarchical clustering of all metabolites (row). Yellow and blue colors indicate increase and decrease of the metabolites scaled to mean and standard deviation of row metabolite level, respectively (see color scale). (D) Categories of all of the identified metabolites.

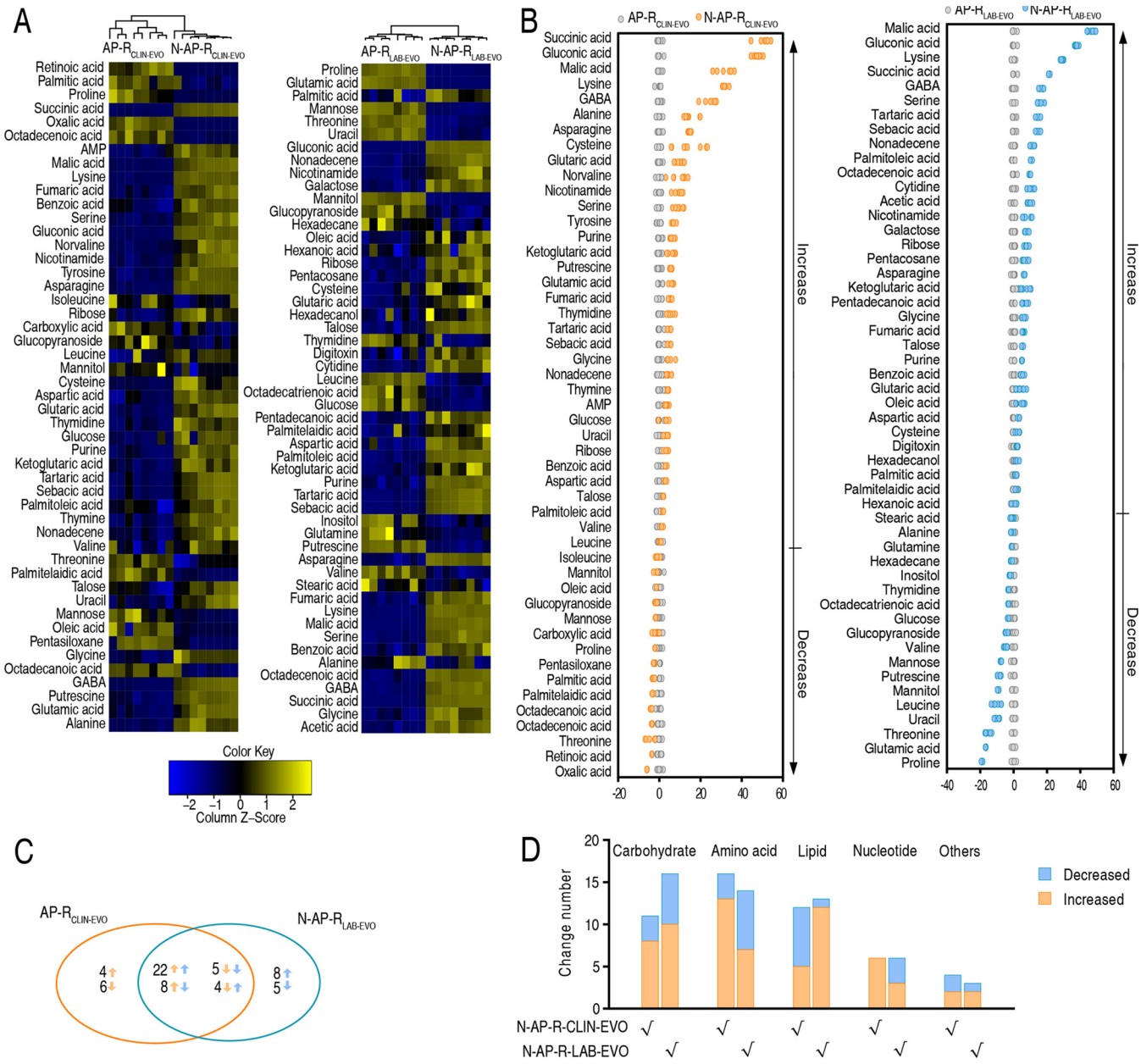

FIG 2 Nitrite-induced differential metabolomics in AP-$R_{CLIN-EVO}$ and AP-$R_{LAB-EVO}$. (A) Heat map showing differential metabolites. The metabolites are organized top to bottom according to hierarchical clustering. Yellow and blue colors indicate increase and decrease of metabolites relative to the median metabolite level, respectively (see color scale). (B) Z-score plot of differential metabolites based on control. The data of AP-$R_{CLIN-EVO}$ (left) and AP-$R_{LAB-EVO}$ (right) groups are separately scaled to the mean and standard deviation of control. Each point represents one metabolite in one technical repeat and colored by sample types. (C) Venn diagram for comparison of nitrite-induced differential metabolites between N-AP-$R_{CLIN-EVO}$ (yellow color) and N-AP-$R_{LAB-EVO}$ (blue color). (D) Number of differential abundance of metabolites.

and other metabolites were 24.29%, 24.29%, 31.43%, 12.86%, and 7.14%, respectively (Fig. 1D). These results indicate that nitrite induces similar metabolic shift between N-AP-$R_{CLIN-EVO}$ and N-AP-$R_{LAB-EVO}$, which is different from AP-$R_{CLIN-EVO}$ and AP-$R_{LAB-EVO}$.

Nitrite-induced differential metabolomes in N-AP-$R_{CLIN-EVO}$ and N-AP-$R_{LAB-EVO}$. A Kruskal–Wallis test ($P < 0.05$) was used to identify metabolites of differential abundance in N-AP-$R_{CLIN-EVO}$ and N-AP-$R_{LAB-EVO}$. Compared with AP-$R_{CLIN-EVO}$ and AP-$R_{LAB-EVO}$, 49 and 52 differential metabolites were detected in N-AP-$R_{CLIN-EVO}$ and N-AP-$R_{LAB-EVO}$, respectively (Fig. 2A). To measure the number of standard deviations between a value and the mean, Z-score calculation was used. It varied between −6.02 and 51.12 in N-AP-$R_{CLIN-EVO}$ and −18.96 and 46.09 in the N-AP-$R_{LAB-EVO}$ group. The top four increased

metabolites were succinic acid, gluconic acid, malic acid, and lysine in N-AP-$R_{CLIN-EVO}$ and malic acid, gluconic acid, lysine, and succinic acid in N-AP-$R_{LAB-EVO}$ (Fig. 2B), where succinic acid and malic acid work for the pyruvate cycle (the P cycle), a recently defined cycle in providing respiratory energy in bacteria (20). Among these differential metabolites, 39 overlapped between the two strains, and 10 and 13 were specific to N-AP-$R_{CLIN-EVO}$ and N-AP-$R_{LAB-EVO}$, respectively. Among the 39 overlapping metabolites, 22 were increased and 5 were decreased in both strains, while 8 were upregulated and 4 were downregulated in N-AP-$R_{CLIN-EVO}$ but oppositely changed in N-AP-$R_{LAB-EVO}$ (Fig. 2C). Number and distribution of these differential abundances of metabolites are shown in Fig. 2D. These results indicate that nitrite induces metabolic shift, where elevated succinic acid and malic acid in the P cycle are a characteristic feature in N-AP-$R_{CLIN-EVO}$ and N-AP-$R_{LAB-EVO}$.

Nitrite-induced pathways in N-AP-$R_{CLIN-EVO}$ and N-AP-$R_{LAB-EVO}$. Pathway enrichment analysis is crucial to cluster the changes in metabolic pathways. Twelve and 13 metabolic pathways were enriched in N-AP-$R_{CLIN-EVO}$ and N-AP-$R_{LAB-EVO}$, respectively, whereas 10 pathways (alanine, aspartate, and glutamate metabolism; lysine degradation; tricarboxylic acid acid [TCA] cycle; glutathione metabolism; arginine biosynthesis; glyoxylate and dicarboxylate metabolism; aminoacyl-tRNA biosynthesis; nicotinate and nicotinamide metabolism; cyanoamino acid metabolism; and taurine and hypotaurine metabolism) overlapped. Besides, valine, leucine, and isoleucine biosynthesis and pantothenate and CoA biosynthesis were enriched in N-AP-$R_{CLIN-EVO}$, while d-glutamine and d-glutamate metabolism, sulfur metabolism, and nitrogen metabolism were enriched in N-AP-$R_{LAB-EVO}$ (Fig. 3A and B). Metabolites in these enriched metabolic pathways are listed in Fig. 3C. Among them, all metabolites of lysine degradation, the TCA cycle, nicotinate and nicotinamide metabolism, and cyanoamino acid metabolism were increased in N-AP-$R_{CLIN-EVO}$ and N-AP-$R_{LAB-EVO}$. Notably, half of the metabolites in lysine degradation and nicotinate and nicotinamide metabolism belong to the TCA cycle (Fig. 3C). Here, we would like to mainly investigate the TCA cycle. Since the P cycle covers the TCA cycle in providing respiratory energy in bacteria (20), the P cycle is used as a key clue for the following study.

Nitrite-induced biomarkers in N-AP-$R_{CLIN-EVO}$ and N-AP-$R_{LAB-EVO}$. Pattern recognition method is a useful tool to identify biomarkers in metabolomics analysis. Thus, orthogonal partial least square discriminant analysis (OPLS-DA) was adopted to recognize the sample patterns of metabolomes. Component t [1] separated N-AP-$R_{CLIN-EVO}$ and N-AP-$R_{LAB-EVO}$ from AP-$R_{CLIN-EVO}$ and AP-$R_{LAB-EVO}$ (Fig. 4A). Furthermore, discriminating variables were demonstrated by S-plot. In the plots of predictive correlation between p [1] and p(corr) [1], the red triangle indicates the differential metabolites that had larger weights (<-0.05 or >0.05) and higher relevance (<-0.5 or >0.5). Fourteen metabolites (alanine, GABA, glutamic acid, glycine, lysine, malic acid, putrescine, succinic acid, octadecanoic acid, oxalic acid, palmitic acid, pentasiloxane, proline, retinoic acid) and 10 metabolites (acetic acid, GABA, glycine, lysine, malic acid, octadecenoic acid, serine, succinic acid, glutamic acid, proline) were identified as biomarkers in N-AP-$R_{CLIN-EVO}$ and N-AP-$R_{LAB-EVO}$, respectively (Fig. 4B). Among them, seven biomarkers overlapped between N-AP-$R_{CLIN-EVO}$ and N-AP-$R_{LAB-EVO}$, and their abundance is shown as scatterplots in Fig. 4C. The presence of malic acid and succinic acid supporting the P cycle may be a key clue to its role in the resistance.

Nitrite-induced metabolic flux in N-AP-$R_{CLIN-EVO}$ and N-AP-$R_{LAB-EVO}$. An online interactive tool, iPath3.0, was used to understand the nitrite-induced global metabolic flux of N-AP-$R_{CLIN-EVO}$ and N-AP-$R_{LAB-EVO}$. Exogenous nitrite activated almost all metabolic pathways, where more activated metabolism was detected in AP-$R_{CLIN-EVO}$ than in AP-$R_{LAB-EVO}$ (Fig. 5A). We further measured activity of pyruvate dehydrogenase (PDH), α-ketoglutarate dehydrogenase (KGDH), succinate dehydrogenase (SDH), and malate dehydrogenase (MDH) in the P cycle to validate the activation of the P cycle. Increased activity of the four enzymes was obtained in N-AP-$R_{CLIN-EVO}$ and N-AP-$R_{LAB-EVO}$ compared with AP-$R_{CLIN-EVO}$ and AP-$R_{LAB-EVO}$, respectively (Fig. 5B). Finally, furfural and malonate, which inhibit the activity of PDH and SDH, respectively, were used to block the P cycle.

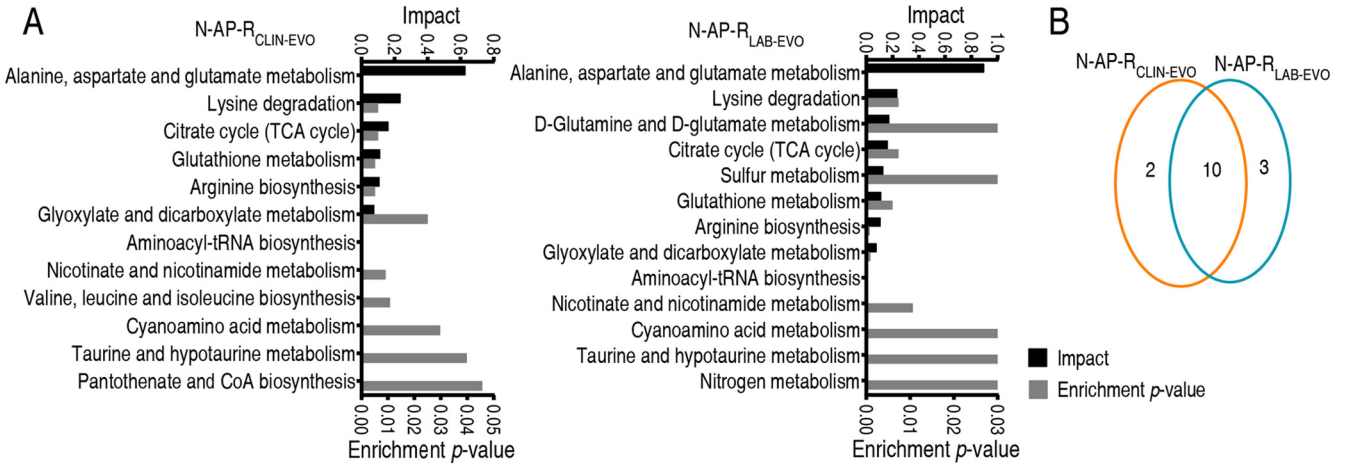

C

Increase
Decrease

	AP-R CLIN-EVO	N-AP-R CLIN-EVO	N-AP-R CLIN-EVO / AP-R CLIN-EVO	AP-R LAB-EVO	N-AP-R LAB-EVO	N-AP-R LAB-EVO / AP-R LAB-EVO
1. Alanine, aspartate and glutamate metabolism						
Aspartic acid	163116	478068	2.93	425885	721237	1.69
Asparagine	877393	1791563	2.04	1231256	1838411	1.49
Alanine	2692985	5799847	2.15	7322011	6433008	0.88
Ketoglutaric acid	319549	559327	1.75	345083	634581	1.84
Glutamic acid	2412808	5812034	2.41	18978685	6480752	0.34
GABA	2182962	8080333	3.70	3928592	10319341	2.63
Glutamine	3628555	3349591	0.92	3672122	3058478	0.83
Fumaric acid	1875064	2564342	1.37	2282396	2656221	1.16
Succinic acid	2478106	18487783	7.46	5351407	15174063	2.84
2. Lysine degradation						
Lysine	487215	3439777	7.06	981844	2988032	3.04
Glutaric acid	116519	337123	2.89	206298	277493	1.35
Ketoglutaric acid	319549	559327	1.75	345083	634581	1.84
Succinic acid	2478106	18487783	7.46	5351407	15174063	2.84
3. Citrate cycle (TCA cycle)						
Ketoglutaric acid	319549	559327	1.75	345083	634581	1.84
Malic acid	476593	2915696	6.12	978478	3258355	3.33
Succinic acid	2478106	18487783	7.46	5351407	15174063	2.84
Fumaric acid	1875064	2564342	1.37	2282396	2656221	1.16
4. Glutathione metabolism						
Glycine	6586365	11697180	1.78	8839708	10921126	1.24
Glutamic acid	2412808	5812034	2.41	18978685	6480752	0.34
Cysteine	141306	566921	4.01	181626	311777	1.72
Putrescine	4104565	6796345	1.66	4177369	3021946	0.72
5. Arginine biosynthesis						
Glutamine	3628555	3349591	0.92	3672122	3058478	0.83
Glutamic acid	2412808	5812034	2.41	18978685	6480752	0.34
Aspartic acid	163116	478068	2.93	425885	721237	1.69
Ketoglutaric acid	319549	559327	1.75	345083	634581	1.84
Fumaric acid	1875064	2564342	1.37	2282396	2656221	1.16
6. Glyoxylate and dicarboxylate metabolism						
Glycine	6586365	11697180	1.78	8839708	10921126	1.24
Glutamic acid	2412808	5812034	2.41	18978685	6480752	0.34
Acetic acid	11160636	9704712	0.87	9418511	12947605	1.37
Succinic acid	2478106	18487783	7.46	5351407	15174063	2.84
Glutamine	3628555	3349591	0.92	3672122	3058478	0.83
Malic acid	476593	2915696	6.12	978478	3258355	3.33
7. Nicotinate and nicotinamide metabolism						
Aspartic acid	163116	478068	2.93	425885	721237	1.69
Fumaric acid	1875064	2564342	1.37	2282396	2656221	1.16
Nicotinamide	840064	1784397	2.12	846671	1428086	1.69
Succinic acid	2478106	18487783	7.46	5351407	15174063	2.84
8. Aminoacyl-tRNA biosynthesis						
Glutamine	3628555	3349591	0.92	3672122	3058478	0.83
Cysteine	141306	566921	4.01	181626	311777	1.72
Glycine	6586365	11697180	1.78	8839708	10921126	1.24
Aspartic acid	163116	478068	2.93	425885	721237	1.69
Valine	985347	1137232	1.15	2129327	1413614	0.66
Alanine	2692985	5799847	2.15	7322011	6433008	0.88
Lysine	487215	3439777	7.06	981844	2988032	3.04
Leucine	294902	384378	1.30	750496	556415	0.74
Threonine	920075	609646	0.66	1544818	858274	0.56
Proline	28011862	20015986	0.71	37860002	17646876	0.47
Glutamic acid	2412808	5812034	2.41	18978685	6480752	0.34
Isoleucine	107663	79980	0.74	34856	34351	0.99
Tyrosine	879046	1641455	1.87	1471594	1495808	1.02
9. Valine, leucine and isoleucine biosynthesis						
Threonine	920075	609646	0.66	1544818	858274	0.56
Leucine	294902	384378	1.30	750496	556415	0.74
Isoleucine	107663	79980	0.74	34856	34351	0.99
Valine	985347	1137232	1.15	2129327	1413614	0.66
10. Cyanoamino acid metabolism						
Asparagine	877393	1791563	2.04	1231256	1838411	1.49
Glycine	6586365	11697180	1.78	8839708	10921126	1.24
Aspartic acid	163116	478068	2.93	425885	721237	1.69
11. Taurine and hypotaurine metabolism						
Glutamic acid	2412808	5812034	2.41	18978685	6480752	0.34
Ketoglutaric acid	319549	559327	1.75	345083	634581	1.84
12. Pantothenate and CoA biosynthesis						
Cysteine	141306	566921	4.01	181626	311777	1.72
Uracil	502920	657964	1.31	1448481	1014578	0.70
Valine	985347	1137232	1.15	2129327	1413614	0.66
13. D-Glutamine and D-glutamate metabolism						
Glutamic acid	2412808	5812034	2.41	18978685	6480752	0.34
Glutamine	3628555	3349591	0.92	3672122	3058478	0.83
14. Sulfur metabolism						
Cysteine	141306	566921	4.01	181626	311777	1.72
Acetic acid	11160636	9704712	0.87	9418511	12947605	1.37
Succinic acid	2478106	18487783	7.46	5351407	15174063	2.84
15. Nitrogen metabolism						
Glutamine	3628555	3349591	0.92	3672122	3058478	0.83
Glutamic acid	2412808	5812034	2.41	18978685	6480752	0.34

FIG 3 Overlapped enriched pathways between N-AP-$R_{CLIN-EVO}$ and N-AP-$R_{LAB-EVO}$. (A) Pathway enrichment of differential metabolites between N-AP-$R_{CLIN-EVO}$ and N-AP-$R_{LAB-EVO}$. (B) Venn diagram for comparison of nitrite-induced pathways between N-AP-$R_{CLIN-EVO}$ (yellow color) and N-AP-$R_{LAB-EVO}$ (blue color). (C) Integrative analysis of metabolites in significantly enriched pathways. Yellow and blue colors indicate increased and decreased metabolites (*P* value <0.05), respectively.

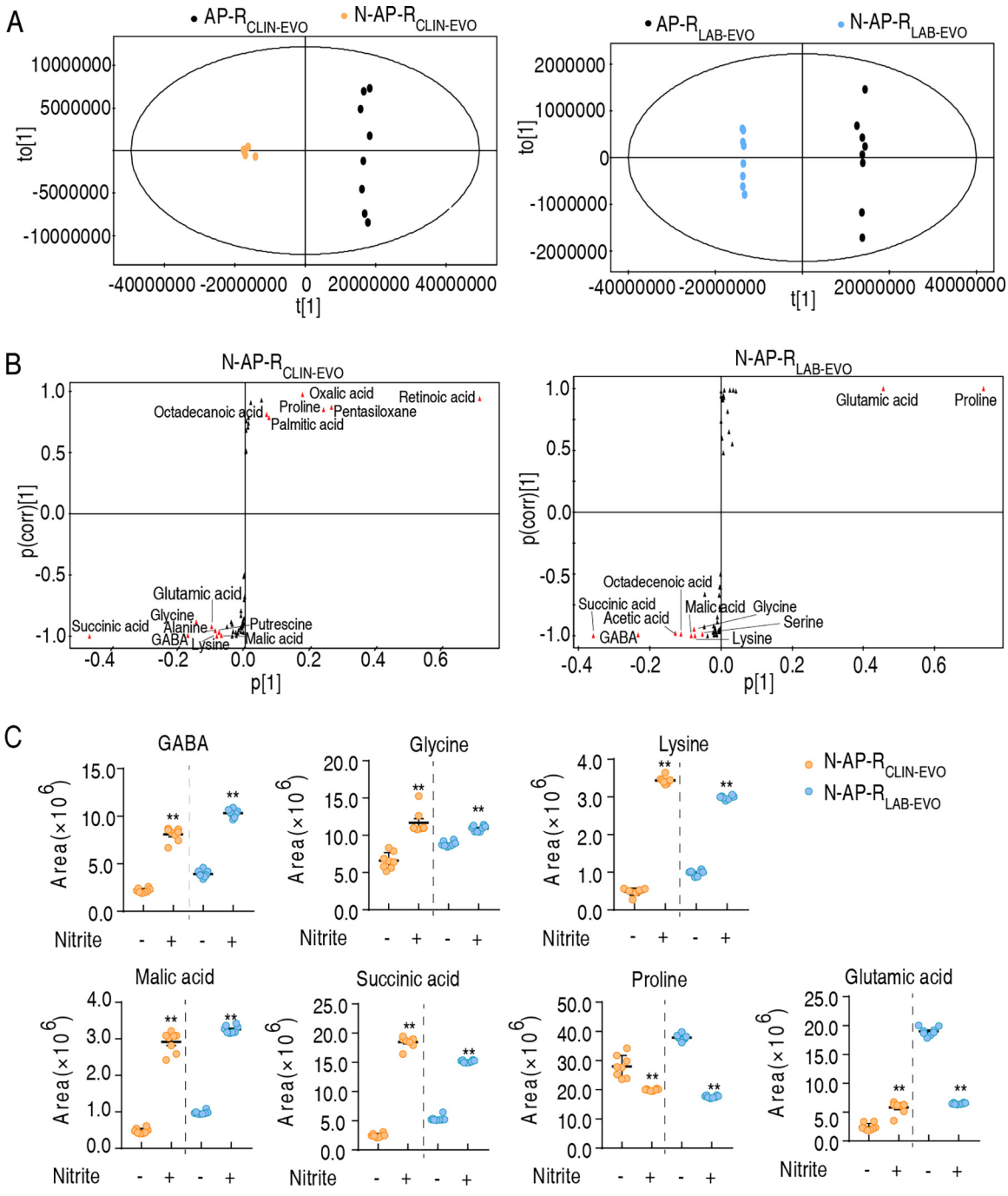

FIG 4 Overlapped biomarkers between N-AP-$R_{CLIN-EVO}$ and N-AP-$_{RLAB-EVO}$. (A) OPLS-DA of nitrite-induced metabolomes in AP-$R_{CLIN-EVO}$ (left) and AP-$_{RLAB-EVO}$ (right). Each dot represents the biological and technical replicate analysis of samples in the plot. (B) S-plot generated from OPLS-DA. Predictive component p [1] and correlation p(corr) [1] differentiate the nitrite-induced group from the control group in AP-$R_{CLIN-EVO}$ (left) and AP-$R_{LAB-EVO}$ (right). Triangles represents individual metabolites, where potential biomarkers are highlighted in red, which are greater or equal to 0.05 and 0.5 for absolute value of covariance p and correlation p(corr), respectively. Otherwise, triangles are marked in black. (C) The scatterplot of overlapped biomarkers of nitrite-induced metabolomes between N-AP-$R_{CLIN-EVO}$ and N-AP-$R_{LAB-EVO}$. Results are displayed as mean ± SEM of four biological replicas and two technical replicates, and significant differences are identified: *, $P < 0.05$; **, $P < 0.01$.

The inhibition elevated the viability of AP-$R_{LAB-EVO}$ and AP-$R_{CLIN-EVO}$ (Fig. 5C). These results validate the activated P cycle as the most characteristic consequence of the nitrite-induced metabolome.

Activation of electron transport chain contributes to nitrite-potentiated SCF killing. Nitrite does not activate the electron transport chain directly (Fig. 6A). Our recent report has indicated that NADH is lower in AP-$R_{CLIN-EVO}$ and AP-$R_{LAB-EVO}$ than their

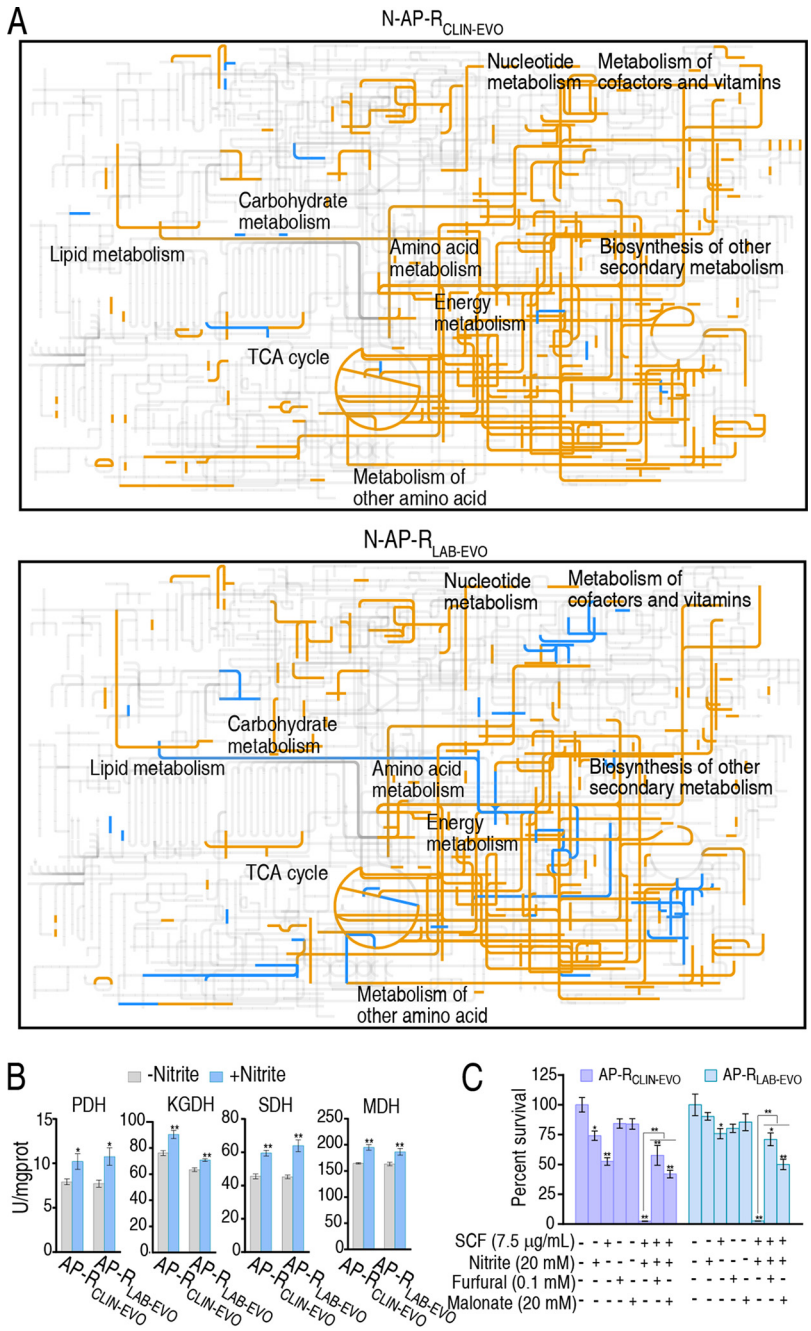

FIG 5 iPath analysis and enzyme activity determination. (A) iPath analysis showing comparison of nitrite-induced metabolomes between N-AP-R$_{CLIN-EVO}$ and N-AP-R$_{LAB-EVO}$. The yellow and blue lines mean upregulation and downregulation of metabolic pathways, respectively. (B) Activity of enzymes of PDH, KGDH, SDH, and MDH in the P cycle with or without nitrite (20 mM). (C) Percent survival of AP-R$_{CLIN-EVO}$ and AP-R$_{LAB-EVO}$ in the presence or absence of furfural or malonate plus SCF and nitrite. Result (C) is obtained using antibiotic bactericidal assay. Results are displayed as mean ± SEM of three biological replicas and significant differences are identified (*, $P < 0.05$; **, $P < 0.01$) as determined by two-tailed Student's *t* test (B) and analysis of variance (ANOVA) (C).

parent strain AP-R$_{CLIN}$, whereas exogenous nitrite promotes higher NADH in AP-R$_{CLIN-EVO}$ and AP-R$_{LAB-EVO}$ than AP-R$_{CLIN}$. Furthermore, nitrite induces expression of Cyt bc1 complex genes (19). Therefore, the activated P cycle should promote electron transport chain. To further demonstrate this, qRT-PCR was used to measure expression of electron transport chain genes in the presence of nitrite. Exogenous nitrite promoted the expression of most genes in N-AP-R$_{CLIN-EVO}$ and N-AP-R$_{LAB-EVO}$. Specifically, expression of

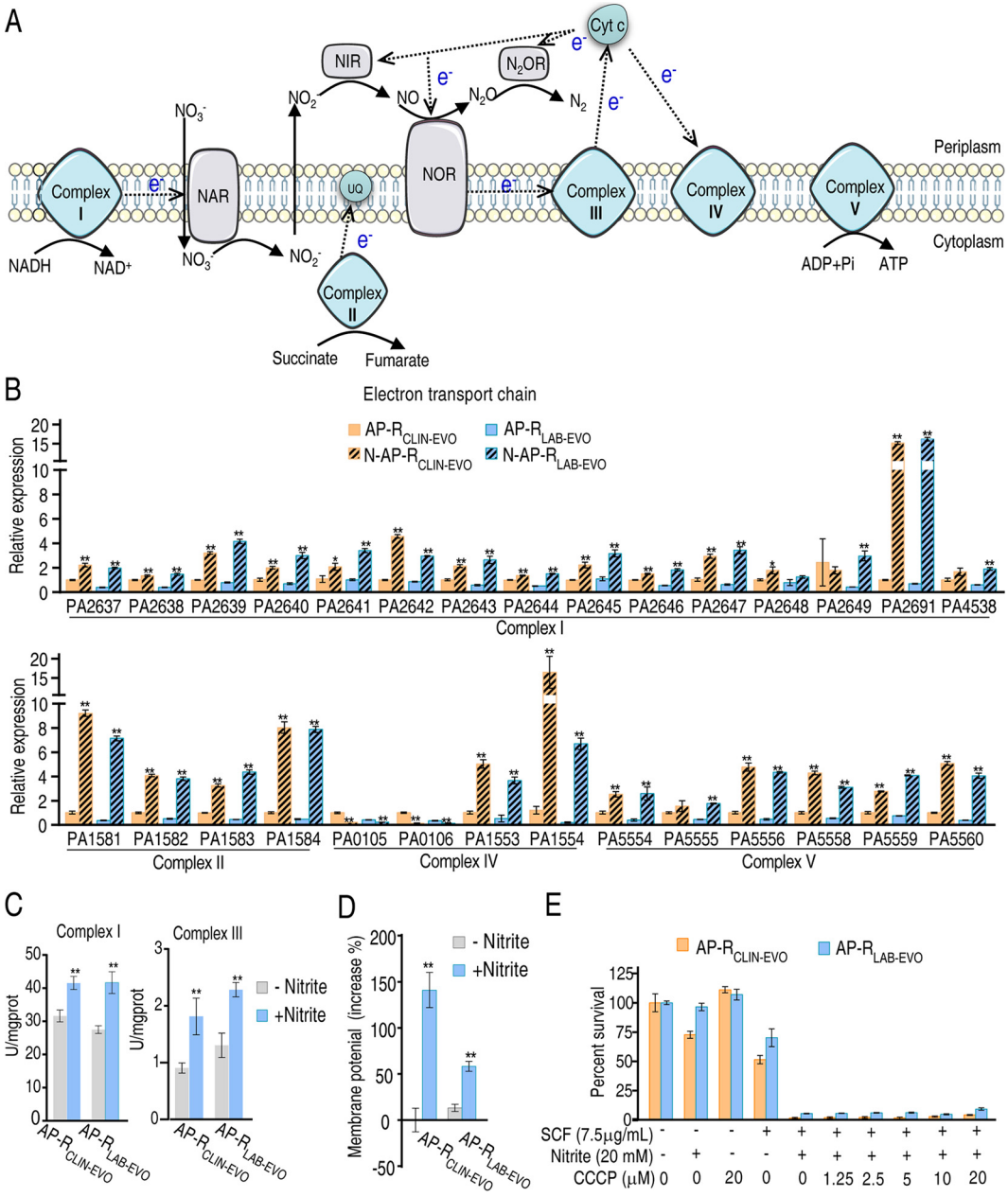

FIG 6 Effect of nitrite on the electron transport chain. (A) Diagram showing electron transport chain. (B) qRT-PCR for expression of genes encoding electron transport chain in the presence of nitrite. (C) Activity of complex II and complex III in electron transport chain in the presence of nitrite (20 mM). (D) Membrane potential in the presence of nitrite. (E) Percent survival of AP-$R_{CLIN-EVO}$ and AP-$R_{LAB-EVO}$ in the presence or absence of the indicated doses of CCCP plus nitrite (20 mM) and SCF (7.5 μg/mL). Result (E) is obtained using antibiotic bactericidal assay. Results are displayed as mean $\pm$ SEM of three (C–E) or four (B) biological replicas, and significant differences are identified (*, $P < 0.05$; **, $P < 0.01$) as determined by two-tailed Student's *t* test.

all genes was upregulated except for PA2648 (unchanged in AP-$R_{LAB-EVO}$) and PA2649 (unchanged in AP-$R_{CLIN-EVO}$) of complex I, and PA0105 and PA0106 (lower in both strains) of complex IV (Fig. 6B). Furthermore, activity of complex 1 and complex III, which generate ROS, was measured. Higher activity of the two enzymes was detected in N-AP-$R_{CLIN-EVO}$ and N-AP-$R_{LAB-EVO}$ than in AP-$R_{CLIN-EVO}$ and AP-$R_{LAB-EVO}$ (Fig. 6C). Exogenous nitrite increased membrane potential (Fig. 6D). However, viability of AP-$R_{CLIN-EVO}$ and AP-$R_{LAB-EVO}$ was similar between the presence and absence of increasing doses of carbonyl cyanide m-chlorophenylhydrazone (CCCP) (Fig. 6E). These results

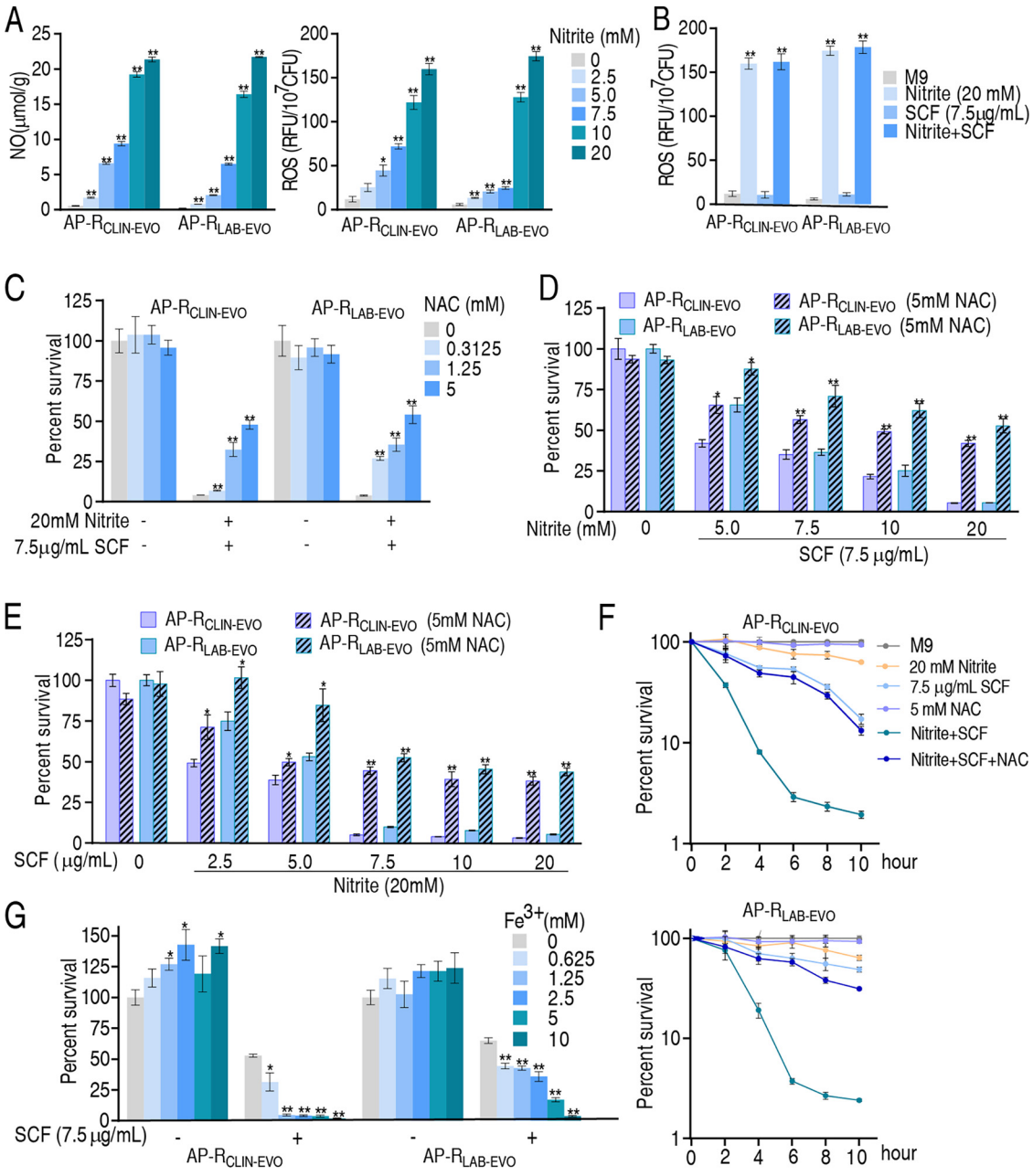

FIG 7 Role of ROS in the synergistic killing of SCF with nitrite. (A) NO and ROS of AP-$R_{CLIN-EVO}$ and AP-$R_{LAB-EVO}$ in the presence of the indicated doses of nitrite. (B) ROS of AP-$R_{CLIN-EVO}$ and AP-$R_{LAB-EVO}$ in the presence of SCF (7.5 μg/mL), nitrite (20 mM), and both. (C) Percent survival of AP-$R_{CLIN-EVO}$ and AP-$R_{LAB-EVO}$ in the indicated concentrations of NAC plus nitrite (20 mM) and SCF (7.5 μg/mL). (D) Percent survival of AP-$R_{CLIN-EVO}$ and AP-$R_{LAB-EVO}$ in the presence or absence of NAC (5 mM) and the indicated concentrations of nitrite plus 7.5 μg/mL SCF. (E) Percent survival of AP-$R_{CLIN-EVO}$ and AP-$R_{LAB-EVO}$ in the presence of NAC (5 mM), nitrite (20 mM), or both plus the indicated concentrations of SCF. (F) Percent survival of AP-$R_{CLIN-EVO}$ and AP-$R_{LAB-EVO}$ in the presence or absence of SCF (7.5 μg/mL), NAC (5 mM), and nitrite (20 mM) at the indicated time point. (G) Percent survival of AP-$R_{CLIN-EVO}$ and AP-$R_{LAB-EVO}$ in the presence or absence of SCF (7.5 μg/mL) and the indicated concentration of Fe^{3+} ($C_6H_{10}FeNO_8$). Results (C–G) are obtained using antibiotic bactericidal assay. Results are displayed as mean ± SEM of three biological replicas, and significant differences are identified (*, $P < 0.05$; **, $P < 0.01$) as determined by analysis of variance (ANOVA).

indicate that nitrite-potentiated SCF-mediated killing is independent of membrane potential.

Activated electron transport chain promotes ROS. It is possible that activation of the electron transport chain elevates ROS. As expected, nitrite promoted not only NO but also ROS of N-AP-$R_{CLIN-EVO}$ and N-AP-$R_{LAB-EVO}$ in a dose-dependent manner. Notably,

A

Name of genes	Entry number	Function	Catalyzed reaction
sodA	PA4468	Superoxide dismutase	2 H^+ + 2 superoxide = H_2O_2 + O_2
sodB	PA4366		
katB	PA4613	Catalase	2 H_2O_2 = 2 H_2O + O_2
katA	PA4236		
katE	PA2147		
trxA	PA5240	Thioredoxin reductase	Thioredoxin + $NADP^+$ = thioredoxin disulfide + NADPH + H^+
trxB	PA2616		
ahpC	PA0139	Peroxiredoxin	NADH + ROOH + H+ = NAD + H_2O + ROH
bcp	PA1008		Thioredoxin + ROOH = thioredoxin disulfide + H_2O + ROH
gshB	PA0407	Glutathione synthetase	ATP + glycine + L- γ-glutamyl-L-cysteine = ADP + glutathione + H^+ + phosphate

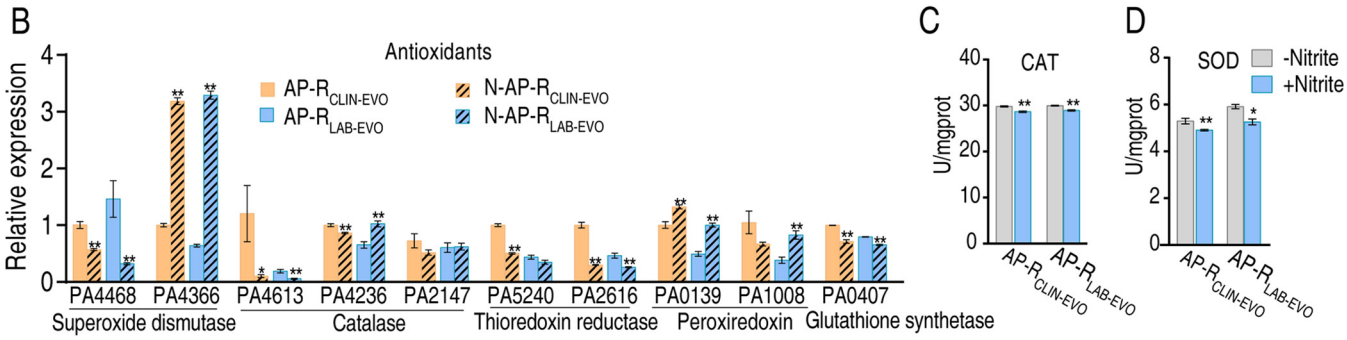

FIG 8 Role of antioxidant in the synergistic killing of SCF with nitrite. (A) Genes with antioxidant functions present in *P. aeruginosa* and the catalyzed reactions of the encoded enzymes. (B) Expression of genes encoding major classes of antioxidants in the presence of nitrite (20 mM). (C and D) Catalase (CAT) activity (C) and SOD activity (D) in the presence of exogenous nitrite (20 mM). Results are displayed as mean ± SEM of three (C and D) or four (B) biological replicas, and significant differences are identified (*, $P < 0.05$; **, $P < 0.01$) as determined by two-tailed Student's *t* test.

NO level was parallel to ROS level (Fig. 7A). However, SCF alone did not increase ROS level and synergize nitrite to increase ROS (Fig. 7B), suggesting that only nitrite is responsible for the elevated ROS. ROS scavenger N-Acetyl-L-cysteine (NAC) rescued the nitrite-potentiated SCF-mediated killing to AP-RCLIN-EVO and AP-RLAB-EVO in a dose-dependent manner (Fig. 7C). Bacterial viability caused by the rescue was reduced with the increasing doses of nitrite or SCF (Fig. 7D and E). The NAC-mediated rescue was enhanced with the incubation time (Fig. 7F). However, Fe^{3+} as a ROS generator promoted SCF-mediated killing to AP-$R_{CLIN-EVO}$ and AP-$R_{LAB-EVO}$ in a dose-dependent manner in addition to its role in increasing growth rates (Fig. 7G). These results indicate that ROS plays a key role in the SCF-mediated killing efficacy.

Nitrite inhibits antioxidants defense system. An antioxidant is an enzyme or cofactor that participates in eliminating ROS. To investigate whether nitrite-induced ROS production was linked to repression of antioxidants, expression of genes encoding antioxidants and activity of their enzymes were measured (Fig. 8A). Among 10 genes encoding five major classes of antioxidants, the expression of 2 genes encoding superoxide dismutase (SOD) was either reduced (PA4468) or increased (PA4366); the expression of three genes encoding catalase (CAT) was decreased (PA4613) and unchanged (PA2147), and reversal change (PA4236); the expression of two genes encoding thioredoxin reductase was decreased (PA5240 and PA2616); the expression of two genes encoding peroxiredoxin was increased (PA0139 and PA1008 only for AP-$R_{LAB-EVO}$); and the expression of one gene encoding glutathione synthetase was decreased (PA0407) in the presence of nitrite (Fig. 8B). Meanwhile, the activity of SOD and CAT was lower in a medium with than without nitrite (Fig. 8C and D). These results indicate that nitrite inhibits degradation of ROS.

H_2O_2 promotes SCF-mediated killing. The above results indicate that nitrite enhances ROS level, which potentiates SCF-mediated killing. Thus, it was necessary to confirm the ROS-potentiated SCF killing. To demonstrate this, H_2O_2 was used. Percent survival of

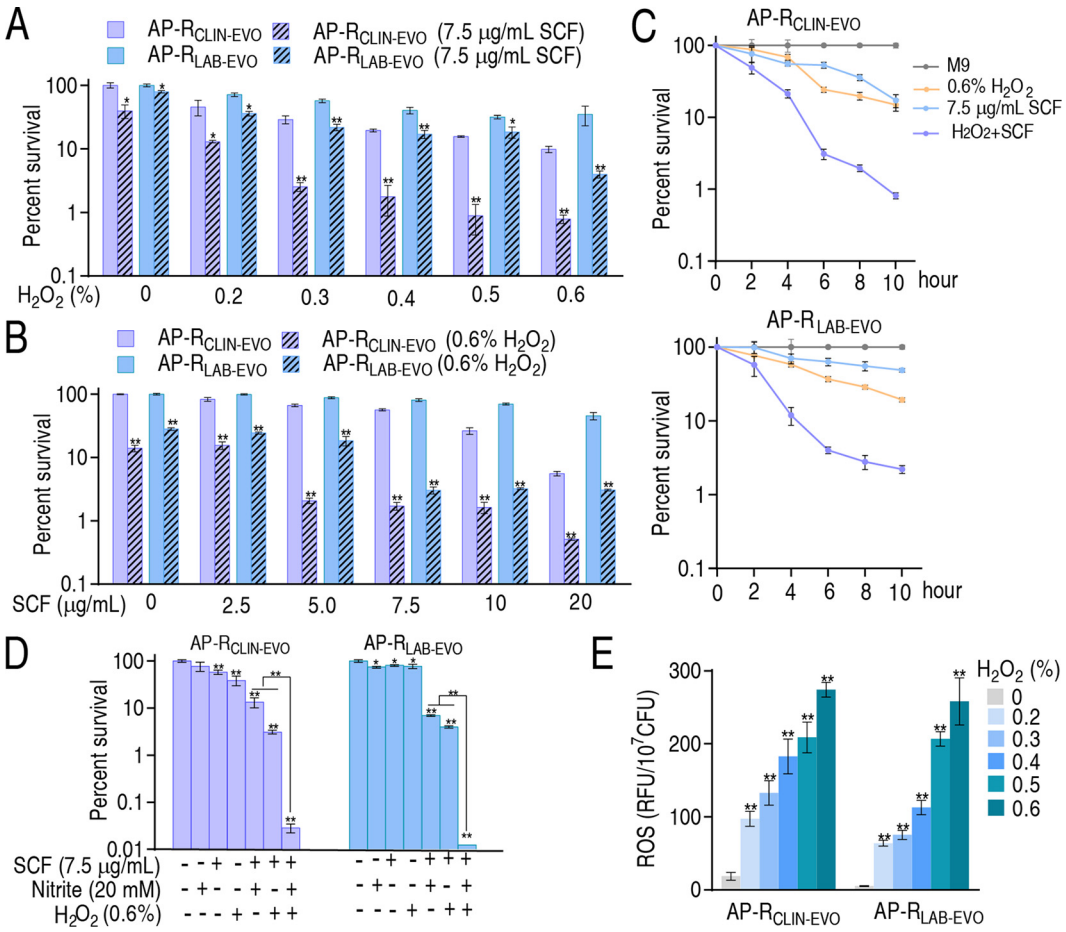

FIG 9 Role of ROS in SCF-mediated killing. (A) Percent survival of AP-$R_{CLIN-EVO}$ and AP-$R_{LAB-EVO}$ in the presence of SCF (7.5 μg/mL) and the indicated concentrations of H_2O_2. (B) Percent survival of AP-$R_{CLIN-EVO}$ and AP-$R_{LAB-EVO}$ in the presence of H_2O_2 (0.6%) and the indicated concentrations of SCF. (C) Percent survival of AP-$R_{CLIN-EVO}$ and AP-$R_{LAB-EVO}$ in the presence of SCF (7.5 μg/mL) and H_2O_2 (0.6%) at the indicated times. (D) Percent survival of AP-$R_{CLIN-EVO}$ and AP-$R_{LAB-EVO}$ in the presence of H_2O_2 (0.6%), nitrite (20 mM), and SCF (7.5 μg/mL). (E) ROS of AP-$R_{CLIN-EVO}$ and AP-$R_{LAB-EVO}$ in the presence of the indicated H_2O_2. Results (A–D) were obtained using antibiotic bactericidal assay. Results are displayed as mean ± SEM of three biological replicas, and significant differences are identified (*, $P < 0.05$; **, $P < 0.01$) as determined by analysis of variance (ANOVA).

AP-$R_{CLIN-EVO}$ and AP-$R_{LAB-EVO}$ was reduced with increasing H_2O_2 concentration when SCF was fixed at 7.5 μg/mL (Fig. 9A). The percent survival was also decreased at 0.6% H_2O_2 in a SCF dose-dependent manner (Fig. 9B). The killing efficacy was increased with the incubation time (Fig. 9C), and the combination of H_2O_2 with the ROS promoted by nitrite (Fig. 9D). The efficacy in 0.6% H_2O_2 was higher than that potentiated by 20 mM nitrite because 0.6% H_2O_2 caused higher ROS than 20 mM nitrite (Fig. 7B and 9E). These results support the conclusion that ROS contributes to SCF-mediated killing.

DISCUSSION

Reprogramming metabolomics is a recently developed approach to promote antibiotic killing efficacy and restore host anti-infective ability through modulation of metabolic states (8, 9, 21–23). The present study uses this approach to understand mechanisms by which nitrite potentiates SCF-mediated killing to AP-$R_{CLIN-EVO}$ and AP-$R_{LAB-EVO}$. It was found that the P cycle and electron transport chain are activated, and thereby ROS is used as an effector to understand the nitrite-potentiated mechanism. Further evidence shows that the elevated ROS contributes to SCF-mediated killing. The finding that nitrite promotes the P cycle and electron transport chain and then increases ROS production to potentiate SCF-mediated killing was previously unknown.

The core finding of the present study is that nitrite activates the P cycle and electron transport chain. It is known that electron transport to nitrite and nitrous oxide involves c-type cytochromes that are to transfer electrons between complex III and complex IV of the respiratory chain (24). Replacement of oxygen by nitrite as final electron acceptor is determined under anaerobic conditions (25). However, whether nitrite activates the P cycle and electron transport chain is unknown except that the Cyt bc1 complex is activated by nitrite (19). Here, the activation of the P cycle is a characteristic feature in nitrite-reprogrammed metabolome, which is further demonstrated by the elevated activity of PDH, KGDH, SDH, and MDH in the P cycle in the presence of nitrite. These findings indicate that exogenous nitrite promotes the P cycle. The activated P cycle provides NADH for the electron transport chain. Further experiments on the expression of genes and the activity of enzymes show that the electron transport chain is activated. The activated electron transport chain elevates membrane potential, but the elevation is not related to SCF-mediated killing. Meanwhile, the activated electron transport chain produces more ROS, which contributes to the killing efficacy. These results also explain our recent finding that the Cyt bc1 complex of the electron transport chain is activated by nitrite (19). Therefore, nitrite activates the electron transport chain through the promotion of the P cycle.

The electron transport chain contributes to ROS production (26). ROS is related to antibiotic sensitivity in various species of bacteria (27–29). For *P. aeruginosa*, oxidative stress increases the development of antibiotic resistance (30, 31), but that ROS potentiates antibiotic-mediated killing efficacy is largely unknown. Kim et al. showed that PA01 is more resistant than PA14 to H_2O_2 as well as to polymyxin B (32). Hayakawa et al. utilized the stimulation by ROS from exposure to 1 mM H_2O_2 and promoted the acquisition of multidrug resistance in 20% of clinical isolates of *P. aeruginosa*. An anti-ROS agent, sodium zinc histidine dithiooctanamide, completely inhibits this acquisition of resistance (30). Liao et al., demonstrated that the mechanism of silver nanoparticles fighting against multidrug-resistant *P. aeruginosa* involves the disequilibrium of oxidation and antioxidation processes and the failure to eliminate the excessive ROS (33). However, polymyxin is not a clinically conventionally used antibiotic, and silver nanoparticles are an antibiotic candidate. The present study indicates that ROS potentiates SCF-mediated killing efficacy to AP-$R_{CLIN-EVO}$ and AP-$R_{LAB-EVO}$. SCF has a better effect against *P. aeruginosa*, *Enterobacteriaceae*, and *Acinetobacter baumannii* than cefoperazone alone and is widely used in clinics (34). Therefore, the elevation of ROS may be a potential approach to potentiate SCF against *P. aeruginosa*. However, AP-$R_{CLIN-EVO}$ and AP-$R_{LAB-EVO}$ originate from the same parent strain AP-R_{CLIN}. Whether the mechanism is common to other clinically isolated multidrug-resistant *P. aeruginosa* strains awaits further investigation on more samples. Notably, ROS level is maintained by both biosynthesis and degradation. To explore whether nitrite breaks this balance, the present study quantifies the expression of genes and the activity of enzymes of the biosynthetic and degradation pathways. Nitrite promotes the biosynthesis of ROS but impairs the degradation pathway. Of note, the biosynthesis of ROS increases more than the degradation. These results suggest that nitrite promoting ROS generation is more crucial for the killing.

Interestingly, ROS is produced by immune cells during bacterial infection (35), which may pose oxidative stress to *P. aeruginosa* during invasion and thereby can be a possible source to facilitate the SCF-mediated killing. Actually, metabolites in alleviating or promoting ROS have been reported from lower vertebrates to *Homo sapiens* (12, 36, 37). Therefore, identifying metabolites promoting both anti-infective immune response and ROS generation can be a promising approach to enhance the killing by SCF, in addition to enhancing immune defense ability during infection, particularly during chronic infection.

In summary, the present study reveals that exogenous nitrite activates the P cycle and electron transport chain, which elevates ROS production. ROS potentiates SCF to kill AP-$R_{CLIN-EVO}$ and AP-$R_{LAB-EVO}$ (Fig. 10). These findings not only identify a previously

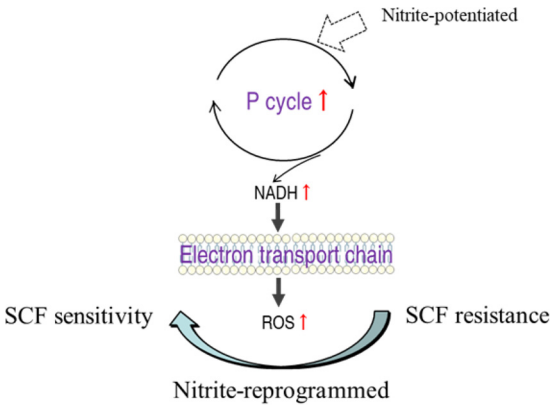

FIG 10 Diagram for the synergistic use of SCF and nitrite to kill AP-$R_{CLIN-EVO}$ and AP-$R_{LAB-EVO}$.

unknown metabolic regulation that nitrite modulates the P cycle and electron transport chain to promote ROS production, but also show that SCF is a ROS-dependent antibiotic.

MATERIALS AND METHODS

Source and culture conditions of bacterial strains. *P. aeruginosa* strains AP-$R_{CLIN-EVO}$ and AP-$R_{LAB-EVO}$ were the same bacteria as the previous report (19) and were kept in our laboratory. These strains were cultured in fresh LB media at 37°C, with 200 rpm shaking until OD_{600} nm of 0.25–0.3. The cultures were reinoculated at 1:1,000 dilutions into 250 mL flasks and incubated for 16 h. The overnight bacteria were collected, washed three times with saline, and suspended in M9 medium (7 g/L K_2HPO_4, 3 g/L KH_2HPO_4, 1 g/L $(NH_4)_2SO_4$, 0.1 g/L $MgSO_4$, 0.588 g/L sodium citrate) to 0.2 of OD_{600} nm when metabolites or/and antibiotics were added if desired. These bacterial cells were cultured at 37°C with 200 rpm for 6 h.

Preparation of samples for nitrite-reprogrammed metabolome and GC-MS analysis. Preparation of samples for nitrite-reprogrammed metabolome was performed as previously described (19). In brief, bacteria were cultured with or without nitrite at 37°C with 200 rpm for 6 h. Then, the bacteria were collected and washed three times with saline. The cells were suspended in saline and adjusted to OD_{600} nm at 1.0. Aliquot of 10 mL cells were collected and transferred to a 1.5 mL centrifuge tube. The cells were immediately quenched with −80°C precooled methanol (HPLC grade). Resuspension of the quenched cells was sonicated for 10 min (200 W total power with 35% output, 2 s pulse, 3 s pause over ice) when 10 μL 0.1 mg/mL ribitol (Sigma) was added as the internal standard. Supernatant was separated by centrifugation at 4°C and 12,000 × *g* for 10 min and placed in a 37°C vacuum centrifuge dryer (Labconco, USA) to evaporate the methanol. The dried samples were added to 80 μL of 20 mg/mL methoximation-pyridine hydrochloride (Sigma-Aldrich) at 37°C and 200 rpm for 3 h. Subsequently, 80 μL of N-methyl-N-trimethylsilyltrifluoroacetamide (MSTFA; Sigma-Aldrich) was added and the reaction was performed at 37°C and 200 rpm for 30 min. The GC-MS data were detected by Agilent 7890A GC equipped with an Agilent 5975C VL MSD detector (Agilent Technologies). The samples of 1 μL were injected into a 30 m × 250 μm i.d. × 0.25 μm DBS-MS column. Initial temperature of the GC oven was held at 85°C for 5 min followed by an increase to 270°C at a rate of 15°C/min and then held for 5 min. Helium was used as the carrier gas and flow was kept constant at 1 mL/min. The MS was operated in a range of 50–600 *m/z*. Each sample was analyzed in four biological repeats with two technical replicas.

Analysis of metabolomic data. Statistical analysis was performed as previously described (38). Briefly, Agilent Chrom Station software (Agilent Technologies, USA) was used to analyze mass fragmentation spectrum and identify compounds thorough matching data with the National Institute of Standards and Technology (NIST) library and NIST MS search 2.0 program. The data were normalized based on total amount of correction and standardized data containing metabolites, retention times, and peak areas, and prepared for further metabolomics analysis. Significant difference of the standardized data was calculated and selected (P value <0.05) by software IBM SPSS Statistics 19. Cluster analysis was carried out by R software (R × 64 3.6.1). Normalized area of differential metabolites was analyzed with Z-score. Principal-component analysis and S-plot analysis were performed by SIMCA-P + 12.0 software (version 12; Umetrics, Umea, Sweden), and the metabolic pathway was done with MetaboAnalyst 4.0 enrichment. Interactive Pathways (iPath) analysis was conducted with iPath 3.0 (https://pathways.embl.de/). Figures were draw by GraphPad Prism 7.0 and Adobe Illustrator CS6.

Detection of nitric oxide. Method for NO content determination under the concentration gradient of nitrite was performed as previously described (19). In brief, bacteria were cultured in M9 medium with or without metabolites at 37°C with 200 rpm for 6 h. Cells were collected and washed three times

with saline. The cells were suspended in saline and adjusted to OD_{600} nm at 1.0. Aliquot of 30 mL cells were collected and transferred to a 1.5 mL centrifuge tube. The cells were resuspended with 0.6 mL saline and disrupted by sonic oscillation for 7 min (200 W total power with 35% output, 2 s pulse, 3 s pause over ice). After centrifugation at 12,000 $\times$ *g* for 10 min at 4°C, supernatants were collected. Protein concentration of the supernatant was quantified by BCA protein concentration determination kit (Beyotime, P0009). Then, 500 μL of 4 mg/mL proteins were mixed with 400 μL buffer I at 37°C for 60 min. The reaction solution was added to 300 μL buffer II, vortexed, and mixed well for 30 s, and then sedimented at 25°C for 40 min. Supernatant was obtained by concentration at 1,600 $\times$ *g* for 10 min. Aliquot of 800 μL supernatant was mixed with 600 μL color developer and sedimented at 25°C for 10 min. Absorbance was measured at 550 nm with a cuvette with 0.5 cm optical path. The same volume of protein buffer and 0.1 mmol/L standard samples were used as a blank control and a reference for concentration calculation, respectively. NO concentration (μmoL/g) was calculated as follows: NO concentration = (Experiment group OD value – blank OD value)/(standard sample OD value – blank OD value) $\times$ standard sample concentration/protein concentration.

Measurement of enzyme activity. Bacteria were cultured in M9 medium with or without nitrite at 37°C with shaking at 200 rpm for 6 h. Cells were collected and immediately snap-frozen in liquid nitrogen and stored at −80°C. The cells were resuspended with 0.5 mL of 1$\times$ PBS and disrupted by sonic oscillation for 5 min (200 W total power with 35% output, 2 s pulse, and 3 s pause over ice). The protein concentration of the supernatant was quantified with a bicinchoninic acid (BCA) kit (Beyotime, P0009, China), and the final protein concentration for each sample was diluted to 3 mg/mL. Complex I activity was determined at 340 nm with a complex I activity assay kit (Solarbio BC 0515, China). Complex III activity was determined at 550 nm with a complex III activity assay kit (Solarbio BC 3240, China). SOD and CAT activity were measured at 450 nm and 405 nm, respectively, using an SOD and CAT assay kit from Nanjing Biomedical Research Institute of Nanjing University (A001-3-2 and A007-1-1, China). PDH, KGDH, SDH, and MDH activities were measured as described previously (19). In brief, a reaction mixture contained 0.15 mM 3-(4,5-dimethyl-2-thiazolyl)-2,5-diphenyl-2H-tetrazolium bromide (MTT), 2.5 mM $MgCl_2$, 6.5 mM phenazine methosulfate (PMS), 0.2 mM thiamine PPi (TPP), and 80 mM sodium pyruvate/alpha-ketoglutaric acid potassium salt for PDH and KGDH activity measurement. Another reaction mixture contained 0.15 mM MTT, 2.5 mM $MgCl_2$, 13 mM PMS, and 80 mM sodium succinate/sodium malate for SDH and MDH activity measurement. Then, the reaction mixtures were incubated at 37°C for 5 min for MDH, PDH, and KGDH, and 10 min for SDH and detected at 562 nm for colorimetric readings. Experiments were repeated in at least three independent biological replicates.

Quantitative real-time PCR. To investigate the effect of nitrite on gene expression levels, quantitative real-time PCR (qRT-PCR) was performed as previously described (39). In brief, after incubation in M9 with or without nitrite at 37°C with 200 rpm for 6 h, cells were collected and adjusted to 1.0 of OD_{600} nm. Total RNA was isolated from 1 mL cell samples by TRIzol reagent (Invitrogen Life Technologies). cDNA was obtained from 1 μg total RNA, and reverse transcription was performed according to a PrimeScript RT reagent kit with gDNA Eraser (Guangzhou IGE Biotechnology Ltd., China). The primers used for qRT-PCR are listed in Table 1, where the 16S rRNA gene served as an internal control. The qRT-PCR was performed in 384-well plates with the SYBR Green Premix Pro *Taq* HS qPCR Kit (Guangzhou IGE Biotechnology Ltd., China) at a total volume of 10 μL. The reaction mixtures were run on a LightCycler 480 system (Roche, Germany). The cycling parameter values were set as follows: 95°C for 30 s to activate the polymerase, 40 cycles of 95°C for 5 s, 58°C for 30 s. Fluorescence measurements were performed at 75°C for 1 s during each cycle. Cycling was terminated at 95°C with a calefactive velocity of 0.11°C s^{-1} to obtain a melting curve. Data were calculated as relative mRNA expression compared to without nitrite group with the endogenous reference 16S rRNA gene.

Antibiotic bactericidal assay. As previously described, antibiotic bactericidal assay was performed in M9 with or without metabolites or/and antibiotics and incubated at 37°C with 200 rpm (40). Six hours later, 100 μL of samples were 10-fold continuously diluted and 10 μL of each dilution was aliquoted on the 2% LB agar plates and cultured at 37°C for about 11 h, and CFU per mL was determined. The percent survival was determined by dividing the CFU obtained from the treated sample by the CFU obtained from the control.

Determination of membrane potential. The membrane potential (PMF) of AP-$R_{CLIN\text{-}EVO}$ and AP-$R_{LAB\text{-}EVO}$ with or without nitrite was measured as follows: bacteria were cultured with or without 20 mM nitrite and incubated at 37°C with 200 rpm for 6 h. Then, the cells were labeled by 3 mM $DiOC_2$ (Sigma) in the dark at 30°C for 30 min. The samples were analyze using a BD FACSCalibur flow cytometer with an excitation wavelength of 488 nm and emission wavelength of 610 nm. Gates for bacterial populations were based on the control population by using forward versus side scatter and red versus green emission. The diverse ratios of red and green indicated fluorescence intensity values of the gated populations. Membrane potential was calculated according to the following: $\log(10^{3/2} \times$ [red fluorescence/green fluorescence]). Three repetitions were performed.

Reactive oxygen species (ROS) assays. ROS assays were performed as follows: bacteria were cultured in M9 with or without metabolites or/and antibiotics at 37°C with 200 rpm for 6 h. A microplate reader was added, and 10^7 CFU cells and 10 μM 2′,7′-dichlorfluorescin diacetate (Sigma) were incubated at 37°C for 30 min in the dark. The samples were analyzed by a Victor X5 multimode plate reader at excitation and emission wavelengths of 485 nm and 535 nm, respectively.

Data availability. All of the metabolomic raw data were deposited to MetaboLights (http://www.ebi.ac.uk/metabolights/) (41). The unique identifier is MTBLS4346.

TABLE 1 Primers for qRT-PCR

Gene	Primer sequence (5′–3′)	Gene	Primer sequence (5′–3′)
16S rRNA-F	CAAAACTACTGAGCTAGAGTACG	PA0105F	CACGGTGGAAATCCTCTGG
16S rRNA-R	TAAGATCTCAAGGATCCCAACGGCT	PA0105R	CGGCTCGGAAGTGTCGTAGAT
PA2637F	GGGGTTTCGTCCCTGCTT	PA0106F	CCTTCGGTGCGGTCAGT
PA2637R	CGATCCGCCAAAGATAGACA	PA0106R	TCAGCGAACCCTCCCACA
PA2638F	CGATAGGCGAACGGGAAAC	PA1553F	TGCCGAGACCGAACGCTAC
PA2638R	GCACGACAGCCCGAAGTTAT	PA1553R	CACGGGTAGGCAGGCATCT
PA2639F	GGCGACCAAGGGTATCAACA	PA1554F	GAATGGGTCTCGGTGTCCT
PA2639R	CCACGTCAGCCATAACGAAA	PA1554R	CAGTTCGGCGTATTCCTTG
PA2640F	CCGACCGTTTCGTCCTCAG	PA5554F	CGTGGGCAAGACCGTCAACA
PA2640R	GACCGATGCCGAGTTGCTT	PA5554R	GGTAGATACCCAGCGAGGC
PA2641F	CGAGATGGAGCCGAACACC	PA5555F	ACGAACCCGACGCCAAGT
PA2641R	AGGGAAGGGCGGTTTGG	PA5555R	TTTCCGAGATTTCCTGGGTG
PA2642F	TGTCTGTCCCTCGGTCTCG	PA5556F	GGAGCAGGATTCCGTGGGT
PA2642R	GTCGTGCGGGTGGTTGGT	PA5556R	GCCGCTGTCTTTCTGGTTG
PA2643F	GCCCAGACCATCTCCTACGA	PA5558F	CCGTTGCGTTCTTCATCTTTG
PA2643R	AGTTCCTGCTCCGCTTCCG	PA5558R	CCTTGACGCTGTTCAGTTCCT
PA2644F	GCTTCGCAGCCTGGTGATG	PA5559F	TGACTGCTATCGCCGTTGC
PA2644R	CGGCTCTTCGGGGTATTGC	PA5559R	TCCAGGAACTTGCCACCC
PA2645F	TGGTTCTGTTCGTCTTCGTGG	PA5560F	CCGCTTCGGGTTACATCCA
PA2645R	CGCCTTGGCATCTACCGTG	PA5560R	CCCATTTCCTTGGCTTGCTC
PA2646F	GATGAGCCTGGAAGTGATGATG	PA4468F	CTTGCCGCCCTTGCCTTAC
PA2646R	GGTGTGGAAGCGGCGATA	PA4468R	TGCCGCAGCAGACTTTCCA
PA2647F	TGCTGCTGTCGTTCTCCCG	PA4366F	AGCCGCACATTTCCGCA
PA2647R	CGTTGTTGCGATTGCTGTAGTA	PA4366R	GGGCTCAGGCAGTTCCAGTA
PA2648F	GGCGTGCTCTCGGTCCTC	PA4613F	GAACGCCTTCCGTCCCG
PA2648R	TTGCCGTCATCGGAACTGT	PA4613R	GCGGATGAAGAAGGTCGGG
PA2649F	TGAACATCTCCCTGAGCGTC	PA4236F	ATGCGACCTTCAAGTGGGA
PA2649R	GCCCCAGTTGAACGGTGC	PA4236R	GGGTAGTCACCGTGGGGC
PA2691F	TGCCCTGATGACCTGCCA	PA2147F	GAAGGGCGACTATCCCGAAT
PA2691R	ATCTTCTTGCCCTCCTCGC	PA2147R	CAGCGGGTCGTTGGTGA
PA4538F	AACCTCACCCACATCTGGAAAC	PA5240F	GCCCTGTGCTGGTGGACT
PA4538R	GATACTCACTGCGTTGTTGTTCG	PA5240R	TTCGGCGGGGTATCCTG
PA1581F	TCAAACTCCCTGTCACCGCT	PA2616F	CCTGGACGAGGTGCTGGG
PA1581R	CACGCTTACCGCCTTCCA	PA2616R	GGTCGGTGTTCGGCTTGTG
PA1582F	TGTCATTTTCCTGCTGGGCT	PA0139F	GCTGCCTTCACCTTCAACTGC
PA1582R	GTCCACATACCGACCCACG	PA0139R	GGACGGAGCGAGGGTCTTCT
PA1583F	CGACCCGAACGACGATTG	PA1008F	CCGACTTCACCGCCCCC
PA1583R	CGAACGGACGCTGGTAGATG	PA1008R	TGGCAGACCGCTTCATCCT
PA1584F	TCAAGGAACAGGACGAGGGC	PA0407F	GATGCCTCCCGCTGGTTC
PA1584R	AGAAGGACGGGCAGGAGG	PA0407R	AACTGCGTGGCGAAGAACT

ACKNOWLEDGMENTS

This work was financially supported by grants from the National Natural Science Foundation of China (No. 82170014) and Guangzhou Science and Technology Plan Project (201904020042). T.-T.Z., Z.-G.C., B.P., X.-X.P., and H.L., wrote the manuscript, interpreted the data, and/or performed the data analysis. T.-T.Z. and Z.-G.C. conceptualized and designed the project. S.F.K., X.L., D.-Y.F., and W.-B.W. performed the experiments. We declare that we have no conflict of interest.

REFERENCES

1. Potron A, Poirel L, Nordmann P. 2015. Emerging broad-spectrum resistance in *Pseudomonas aeruginosa* and *Acinetobacter baumannii*: mechanisms and epidemiology. Int J Antimicrob Agents 45:568–585. https://doi.org/10.1016/j.ijantimicag.2015.03.001.
2. Olga P, Apostolos V, Alexis G, George V, Athena M. 2016. Antibiotic resistance profiles of *Pseudomonas aeruginosa* isolated from various Greek aquatic environments. FEMS Microbiol Ecol 92:fiw042. https://doi.org/10.1093/femsec/fiw042.
3. Mielko K, Jabłoński S, Milczewska J, Sands D, Łukaszewicz M, Młynarz P. 2019. Metabolomic studies of *Pseudomonas aeruginosa*. World J Microbiol Biotechnol 35:178. https://doi.org/10.1007/s11274-019-2739-1.
4. Han M, Zhu Y, Creek D, Lin YW, Anderson D, Shen H, Tsuji B, Gutu A, Moskowitz S, Velkov T, Li J. 2018. Alterations of metabolic and lipid profiles in polymyxin-resistant *Pseudomonas aeruginosa*. Antimicrob Agents Chemother 62:e02656-17. https://doi.org/10.1128/AAC.02656-17.
5. Han M, Zhu Y, Creek D, Lin Y, Gutu A, Hertzog P, Purcell T, Shen H, Moskowitz S, Velkov T, Li J. 2019. Comparative metabolomics and transcriptomics reveal multiple pathways associated with polymyxin killing in *Pseudomonas aeruginosa*. mSystems 4:e00149-18. https://doi.org/10.1128/mSystems.00149-18.
6. Hussein M, Han M, Zhu Y, Schneider-Futschik E, Hu X, Zhou Q, Lin Y, Anderson D, Creek D, Hoyer D, Li J, Velkov T. 2018. Mechanistic insights from global metabolomics studies into synergistic bactericidal effect of a polymyxin B combination with tamoxifen against cystic fibrosis MDR *Pseudomonas aeruginosa*. Comput Struct Biotechnol J 16:587–599. https://doi.org/10.1016/j.csbj.2018.11.001.

7. Hussein M, Schneider-Futschik E, Paulin O, Allobawi R, Crawford S, Zhou Q, Hanif A, Baker M, Zhu Y, Li J, Velkov T. 2020. Effective strategy targeting polymyxin-resistant gram-negative pathogens: polymyxin B in combination with the selective serotonin reuptake inhibitor sertraline. ACS Infect Dis 6:1436–1450. https://doi.org/10.1021/acsinfecdis.0c00108.
8. Peng B, Li H, Peng X. 2015. Functional metabolomics: from biomarker discovery to metabolome reprogramming. Protein Cell 6:628–637. https://doi.org/10.1007/s13238-015-0185-x.
9. Peng B, Su Y, Li H, Han Y, Guo C, Tian Y, Peng X. 2015. Exogenous alanine and/or glucose plus kanamycin kills antibiotic-resistant bacteria. Cell Metab 21:249–262. https://doi.org/10.1016/j.cmet.2015.01.008.
10. Jiang M, Kuang S, Lai S, Zhang S, Yang J, Peng B, Peng X, Chen Z, Li H. 2020. Na^+-NQR confers aminoglycoside resistance via the regulation of L-alanine metabolism. mBio 11:e02086-20. https://doi.org/10.1128/mBio.02086-20.
11. Yang D, Yang H, Cao Y, Jiang M, Zheng J, Peng B. 2021. Succinate promotes phagocytosis of monocytes/macrophages in teleost fish. Front Mol Biosci 8:644957. https://doi.org/10.3389/fmolb.2021.644957.
12. Yang D, Yang M, Yin Y, Kou T, Peng L, Chen Z, Zheng J, Peng B. 2021. Serine metabolism tunes immune responses to promote *Oreochromis niloticus* survival upon *Edwardsiella tarda* infection. mSystems 6:e0042621. https://doi.org/10.1128/mSystems.00426-21.
13. Cheng Z, Guo C, Chen Z, Yang T, Zhang J, Wang J, Zhu J, Li D, Zhang T, Li H, Peng B, Peng X. 2019. Glycine, serine and threonine metabolism confounds efficacy of complement-mediated killing. Nat Commun 10:3325. https://doi.org/10.1038/s41467-019-11129-5.
14. Zhang S, Wang J, Jiang M, Xu D, Peng B, Peng X, Li H. 2019. Reduced redox-dependent mechanism and glucose-mediated reversal in gentamicin-resistant *Vibrio alginolyticus*. Environ Microbiol 21:4724–4739. https://doi.org/10.1111/1462-2920.14811.
15. Zhao XL, Chen ZG, Yang TC, Jiang M, Wang J, Cheng ZX, Yang MJ, Zhu JX, Zhang TT, Li H, Peng B, Peng XX. 2021. Glutamine promotes antibiotic uptake to kill multidrug-resistant uropathogenic bacteria. Sci Transl Med 13:eabj0716. https://doi.org/10.1126/scitranslmed.abj0716.
16. Zhang S, Yang M, Peng B, Peng X, Li H. 2020. Reduced ROS-mediated antibiotic resistance and its reverting by glucose in *Vibrio alginolyticus*. Environ Microbiol 22:4367–4380. https://doi.org/10.1111/1462-2920.15085.
17. Wang Q, Lin M, Shen P, Guan Y. 2021. Elevation of fatty acid biosynthesis metabolism contributes to zhongshengmycin resistance in *Xanthomonas oryzae*. Antibiotics (Basel) 10:1166. https://doi.org/10.3390/antibiotics10101166.
18. Kuang S, Chen Y, Chen J, Peng X, Chen Z, Li H. 2021. Synergy of alanine and gentamicin to reduce nitric oxide for elevating killing efficacy to antibiotic-resistant *Vibrio alginolyticus*. Virulence 12:1737–1753. https://doi.org/10.1080/21505594.2021.1947447.
19. Kuang S, Feng D, Chen Z, Liang Z, Xiang J, Li H, Peng X, Zhang T. 2021. Inactivation of nitrite-dependent nitric oxide biosynthesis is responsible for overlapped antibiotic resistance between naturally and artificially evolved *Pseudomonas aeruginosa*. mSystems 6:e00732-21. https://doi.org/10.1128/mSystems.00732-21.
20. Su Y, Kuang S, Ye J, Tao J, Li H, Peng X, Peng B. 2021. Enhanced biosynthesis of fatty acids is associated with the acquisition of ciprofloxacin resistance in *Edwardsiella tarda*. mSystems 6:e0069421. https://doi.org/10.1128/mSystems.00694-21.
21. Jiang M, Chen Z, Zheng J, Peng B. 2019. Metabolites-enabled survival of crucian carps infected by *Edwardsiella tarda* in high water temperature. Front Immunol 10:1991. https://doi.org/10.3389/fimmu.2019.01991.
22. Jiang M, Yang L-F, Zheng J, Chen Z-G, Peng B. 2020. Maltose promotes crucian carp survival against *Aeromonas sobrial* infection at high temperature. Virulence 11:877–888. https://doi.org/10.1080/21505594.2020.1787604.
23. Jiang M, Yang L, Chen Z, Lai S, Zheng J, Peng B. 2020. Exogenous maltose enhances zebrafish immunity to levofloxacin-resistant *Vibrio alginolyticus*. Microb Biotechnol 13:1213–1227. https://doi.org/10.1111/1751-7915.13582.
24. Hough M, Silkstone G, Worrall J, Wilson M. 2014. NO binding to the proapoptotic cytochrome c-cardiolipin complex. Vitam Horm 96:193–209. https://doi.org/10.1016/B978-0-12-800254-4.00008-8.
25. Borrero-de Acuña J, Timmis K, Jahn M, Jahn D. 2017. Protein complex formation during denitrification by *Pseudomonas aeruginosa*. Microb Biotechnol 10:1523–1534. https://doi.org/10.1111/1751-7915.12851.
26. Galván A, Chalón M, Schurig-Briccio L, Salomón R, Minahk C, Gennis R, Bellomio A. 2018. Cytochromes *bd*-I and bo_3 are essential for the bactericidal effect of microcin J25 on *Escherichia coli* cells. Biochim Biophys Acta Bioenerg 1859:110–118. https://doi.org/10.1016/j.bbabio.2017.10.006.
27. Kohanski M, DePristo M, Collins J. 2010. Sublethal antibiotic treatment leads to multidrug resistance via radical-induced mutagenesis. Mol Cell 37:311–320. https://doi.org/10.1016/j.molcel.2010.01.003.
28. Brynildsen M, Winkler J, Spina C, MacDonald I, Collins J. 2013. Potentiating antibacterial activity by predictably enhancing endogenous microbial ROS production. Nat Biotechnol 31:160–165. https://doi.org/10.1038/nbt.2458.
29. Ye J, Su Y, Lin X, Lai S, Li W, Ali F, Zheng J, Peng B. 2018. Alanine enhances aminoglycosides-induced ROS production as revealed by proteomic analysis. Front Microbiol 9:29. https://doi.org/10.3389/fmicb.2018.00029.
30. Hayakawa S, Kawamura M, Sato T, Hirano T, Kikuchi T, Watanabe A, Fujimura S. 2019. An α-Lipoic acid derivative, and anti-ROS agent, prevents the acquisition of multi-drug resistance in clinical isolates of *Pseudomonas aeruginosa*. J Infect Chemother 25:28–33. https://doi.org/10.1016/j.jiac.2018.10.003.
31. Ahmed M, Porse A, Abdelsamad A, Sommer M, Høiby N, Ciofu O. 2019. Lack of the major multifunctional catalase KatA in *Pseudomonas aeruginosa* accelerates evolution of antibiotic resistance in ciprofloxacin-treated biofilms. Antimicrob Agents Chemother 63:e00766-19. https://doi.org/10.1128/AAC.00766-19.
32. Kim B, Chung I, Cho Y. 2019. Differential expression of the major catalase, KatA in the two wild type *Pseudomonas aeruginosa* strains, PAO1 and PA14. J Microbiol 57:704–710. https://doi.org/10.1007/s12275-019-9225-1.
33. Liao S, Zhang Y, Pan X, Zhu F, Jiang C, Liu Q, Cheng Z, Dai G, Wu G, Wang L, Chen L. 2019. Antibacterial activity and mechanism of silver nanoparticles against multidrug-resistant *Pseudomonas aeruginosa*. IJN 14:1469–1487. https://doi.org/10.2147/IJN.S191340.
34. Ku Y, Yu W. 2021. Cefoperazone/sulbactam: new composites against multiresistant gram negative bacteria? Infect Genet Evol 88:104707. https://doi.org/10.1016/j.meegid.2021.104707.
35. Pestrak MJ, Chaney SB, Eggleston HC, Dellos-Nolan S, Dixit S, Mathew-Steiner SS, Roy S, Parsek MR, Sen CK, Wozniak DJ. 2018. *Pseudomonas aeruginosa* rugose small-colony variants evade host clearance, are hyperinflammatory, and persist in multiple host environments. PLoS Pathog 14:e1006842. https://doi.org/10.1371/journal.ppat.1006842.
36. Peng HY, Lucavs J, Ballard D, Das JK, Kumar A, Wang L, Ren Y, Xiong X, Song J. 2021. Metabolic reprogramming and reactive oxygen species in T cell immunity. Front Immunol 12:652687. https://doi.org/10.3389/fimmu.2021.652687.
37. Gong QY, Yang MJ, Yang LF, Chen ZG, Jiang M, Peng B. 2020. Metabolic modulation of redox state confounds fish survival against *Vibrio alginolyticus* infection. Microb Biotechnol 13:796–812. https://doi.org/10.1111/1751-7915.13553.
38. Su Y, Peng B, Li H, Cheng Z, Zhang T, Zhu J, Li D, Li M, Ye J, Du C, Zhang S, Zhao X, Yang M, Peng X. 2018. The pyruvate cycle increases aminoglycosides efficacy and provides respiratory energy in bacteria. Proc Natl Acad Sci U S A 115:E1578–E1587. https://doi.org/10.1073/pnas.1714645115.
39. Wang Y, Wang X, Ali F, Li Z, Fu Y, Yang X, Lin W, Lin X. 2019. Comparative extracellular proteomics of *Aeromonas hydrophila* reveals iron-regulated secreted proteins as potential vaccine candidates. Front Immunol 10:256. https://doi.org/10.3389/fimmu.2019.00256.
40. Zhao Y, Lv B, Sun F, Liu J, Wang Y, Gao Y, Qi F, Chang Z, Fu X. 2020. Rapid freezing enables aminoglycosides to eradicate bacterial persisters via enhancing mechanosensitive channel MscL-mediated antibiotic uptake. mBio 11:e03239-19. https://doi.org/10.1128/mBio.03239-19.
41. Haug K, Cochrane K, Nainala VC, Williams M, Chang J, Jayaseelan KV, O'Donovan C. 2020. MetaboLights: a resource evolving in response to the needs of its scientific community. Nucleic Acids Res 48:D440–D444. https://doi.org/10.1093/nar/gkz1019.